ADVANCED OPTICAL MATERIALS
www.advopticalmat.de

Beyond the Energy Gap Law: The Influence of Selection Rules and Host Compound Effects on Nonradiative Transition Rates in Boltzmann Thermometers

Philip Netzsch, Matthias Hämmer, Erich Turgunbajew, Thomas P. van Swieten, Andries Meijerink, Henning A. Höppe,* and Markus Suta**

Apart from the energy gap law, control parameters over nonradiative transitions are so far only scarcely regarded. In this work, the impact of both covalence of the lanthanoid–ligand bond and varying bond distance on the magnitude of the intrinsic nonradiative decay rate between the excited $^6P_{5/2}$ and $^6P_{7/2}$ spin–orbit levels of Gd^{3+} is investigated in the chemically related compounds $Y_2[B_2(SO_4)_6]$ and $LaBO_3$. Analysis of the temperature-dependent luminescence spectra reveals that the intrinsic nonradiative transition rates between the excited ^6P_J (J = 5/2, 7/2) levels are of the order of only 10 ms^{-1} ($Y_2[B_2(SO_4)_6]:Gd^{3+}$: 8.9 ms^{-1}; $LaBO_3:Gd^{3+}$: 10.5 ms^{-1}) and differ due to the different degree of covalence of the Gd—O bonds in the two compounds. Comparison to the established luminescent Boltzmann thermometer Er^{3+} reveals, however, that the nonradiative transition rates between the excited levels of Gd^{3+} are over three orders of magnitude slower despite a similar energy gap and the presence of a single resonant phonon mode. This hints to a fundamental magnetic dipolar character of the nonradiative coupling in Gd^{3+}. These findings can pave a way to control nonradiative transition rates and how to tune the dynamic range of luminescent Boltzmann thermometers.

1. Introduction

Remote temperature sensing with noninvasive optical methods becomes increasingly popular.[1–4] Potential application areas range from biothermal imaging,[5,6] temperature monitoring in catalysis,[7–10] microelectronics,[11] or molecular logics[12] to the investigation of fundamental thermodynamic phenomena[13] at the micro- and nanoscale. One of the conceptually simplest ways of optical temperature sensing, also in terms of the required setup, is the exploitation of the luminescence intensity ratio (LIR) of two emission bands due to radiative transitions from two thermally coupled excited levels of an ensemble of non-interacting ions. In case of efficient thermal coupling between these levels by (multi) phonon transitions, the LIR follows Boltzmann's law.[14] Trivalent lanthanoid ions with the rich energy level structure arising from their partially filled $4f^n$ (n = 1–13) configuration are primary representatives for this type of luminescence thermometry, with Er^{3+} and its green-emitting $^2H_{11/2}$ and $^4S_{3/2}$ levels being the most prominent examples.[7,15]

Boltzmann-type equilibrium between the two excited levels critically depends on the interplay between the depopulating radiative decay and the nonradiative multiphonon thermalization pathways.[14,16] The rate-determining step is the

P. Netzsch, M. Hämmer, E. Turgunbajew, H. A. Höppe
Lehrstuhl für Festkörperchemie
Universität Augsburg
86159 Augsburg, Germany
E-mail: henning@ak-hoeppe.de

P. Netzsch
School of Chemistry
University of St. Andrews
North Haugh, St Andrews KY16 9ST, UK

The ORCID identification number(s) for the author(s) of this article can be found under https://doi.org/10.1002/adom.202200059.

DOI: 10.1002/adom.202200059

T. P. van Swieten, A. Meijerink
Condensed Matter & Interfaces
Debye Institute for Nanomaterials Science
Department of Chemistry
Utrecht University
Princetonplein 1, Utrecht 3584CC, The Netherlands
E-mail: a.meijerink@uu.nl

M. Suta
Inorganic Photoactive Materials
Institute of Inorganic Chemistry
Heinrich Heine University Düsseldorf
Universitätsstraße 1, 40225 Düsseldorf, Germany
E-mail: markus.suta@hhu.de

nonradiative absorption from the lower-excited to the higher-excited emissive level, which competes with radiative or any additional quenching transition.[17,18] Only if the nonradiative thermalization is much faster than any depopulation channel of the excited levels, Boltzmann equilibrium is sustained and, thus, luminescence thermometry can be performed.[14,16] Otherwise, the two excited levels decouple, and the Boltzmann temperature sensing concept is invalidated. While control over the radiative decay rate has opened a whole scientific branch of photonics and includes ways of local electric field enhancement in, e.g., nanocrystals immersed in strongly dielectric media,[19] or local density of states enhancement by the Purcell effect in a small high-quality cavity,[20] control over the nonradiative transition rates has not been as well established so far. It has been both experimentally and theoretically realized that the intrinsic nonradiative multiphonon decay rate from a higher excited level roughly scales exponentially with the number of required effective phonon modes to bridge an energy gap between two electronic states, which is commonly referred to as the energy gap law.[21–23] Ermolaev and Sveshnikova[24,25] as well as van Dijk and Schuurmans,[26] later indicated that the nonradiative transition rate could also be dependent on the lanthanoid–ligand distances in a host compound. The former authors interpreted the nonradiative transition as a resonant Förster-type energy transfer between the transition dipole moment coupling the two electronic levels and the vibrational mode of a surrounding solvent molecule resonant with the energy gap. This was recently used to explain and model solvent quenching and the reduced upconversion efficiency of β-$NaYF_4$:Er^{3+}, Yb^{3+} upconversion nanocrystals compared to microcrystals.[27] Van Dijk and Schuurmans explained the expected distance dependence of the intrinsic nonradiative decay rate in terms of a multipole expansion.[26] Some of us have recently proposed an alternative view on a nonradiative rate that would intuitively allow us to distinguish between electric and magnetic dipolar-type nonradiative transitions. Here, the collective vibrational motion of the surrounding ligands serves as a source for induced electromagnetic fields due to the acceleration of charge density to which the transition dipole moment between the two electronic levels can couple, thus mediating the nonradiative transition.[14] This model also allows us to explicitly distinguish electric and magnetic dipolar transitions by means of the distance dependence of the respective nonradiative rate. For the idealized case of coupled point dipoles, electric-dipole-type nonradiative transitions expectedly follow a d^{-6} dependence with d as the metal–ligand distance, similarly to what the Förster-type energy transfer model by Ermolaev and Sveshnikova predicts, while magnetic dipolar nonradiative transitions should depend on the metal–ligand distance as d^{-4}. In addition, magnetic dipolar nonradiative transitions are expected to be much slower (by a factor of around 10^{-4}–10^{-5}) due to the much weaker induced magnetic field by the vibrational motion of the surrounding ligands in the near field.[14,24,25] A similar concept of selection rules for nonradiative transitions is known for intersystem crossing in organic molecules in terms of El-Sayed's rules, which state that intersystem crossing becomes fast if the type (and thus, the orbital angular momentum projection on a defined molecular axis) of molecular orbital changes during this transition to conserve total angular momentum.[28]

While the concepts for nonradiative transitions of the lanthanoid ions are theoretically established, they still lack experimental evidence. So far, it has only been demonstrated that the energy transfer-type interpretation of nonradiative transitions works well to explain the quenching behavior in different solvents for lanthanoid-based coordination compounds or lanthanoid-doped nanocrystals.[24,25,27,29] Evidence for the validity of the previously described models would be an experimentally observed dependence of the intrinsic nonradiative decay rate on the metal–ligand distance d and a significant difference between magnetic and electric-dipole-type nonradiative transition rates. An experimental verification of these concepts and better fundamental understanding of the nature of the nonradiative rates provide insights that help steer the thermal sensing behavior of lanthanoid ions by variation of the local surroundings in a host compound.

In this work, these theoretical considerations are experimentally verified for the case of nonradiative coupling of the UV-emitting ^6P_J (J = 5/2, 7/2) levels of Gd^{3+}. This ion is an ideal model system to address these questions because it has no additional electronic levels between the ^6P_J levels and the $^8S_{7/2}$ ground level. Gd^{3+} was doped into borosulfate $Y_2[B_2(SO_4)_6]$ and orthoborate $LaBO_3$. Both compounds offer similar low symmetric coordination spheres for the incorporated Gd^{3+} ions to avoid any potential impact of symmetry-based selection rules. Orthoborates are well-known host compounds for lanthanoid ions. In contrast, borosulfates are not as well known and have a so-called weak coordination behavior due to the additional electron-withdrawing character of the sulfate groups containing S(VI).[30,31] Thus, these compounds are ideally suited to simultaneously test the counteracting impacts of the chemical nature on the one hand, and the length of the lanthanoid–ligand bond, on the other hand, on the intrinsic nonradiative rate coupling two excited levels.

2. Results and Discussion

2.1. Crystal Structures of $LaBO_3$ and $Y_2[B_2(SO_4)_6]$

$LaBO_3$ crystallizes in an aragonite ($CaCO_3$)-type structure in the orthorhombic crystal system with space group *Pnma* (No. 62).[32] The lanthanum atoms occupy the special 4*c* Wyckoff positions and are ninefold coordinated by oxygen atoms in form of a distorted tricapped trigonal prism with C_s site symmetry. $Y_2[B_2(SO_4)_6]$ crystallizes in the $Gd_2[B_2(SO_4)_6]$ structure type[33] in the monoclinic crystal system with space group $C2/c$ (No. 15).[30] The yttrium atoms are located on the general 8*f* Wyckoff sites and are eightfold coordinated by oxygen atoms in form of an approximate square antiprism with C_1 site symmetry. Given the more Lewis-acidic nature of the attached sulfate groups around the yttrium atom in the borosulfate compared to the oxidoborate groups around the lanthanum atom in the orthoborate, the oxygen ligands expectedly have a weaker σ-donating character in the borosulfate compound. This introduces a lower degree of covalency of a lanthanoid–oxygen interaction in the borosulfates, which results in a rather weak coordination strength. On the other hand, La^{3+} has a larger ionic radius than Y^{3+}, which renders the average

La—O bond lengths in $LaBO_3$ longer than the Y—O bond lengths in $Y_2[B_2(SO_4)_6]$. Since the crystal structures of other aragonite-type lanthanoid orthoborates $LnBO_3$ (Ln = Ce, Pr, and Nd) were refined much more reliably from powder,[34,35] or single-crystal X-ray diffraction,[36,37] data at room temperature than $LaBO_3$ and show a linear correlation with the ionic radius of the lanthanoid ions, the average La—O bond length in $LaBO_3$ at room temperature was estimated by extrapolation yielding $\langle d_{La-O} \rangle$ = (2.581 ± 0.050) Å. The average Y—O bond length in $Y_2[B_2(SO_4)_6]$ based on single-crystal structure data at room temperature is $\langle d_{Y-O} \rangle$ = (2.346 ± 0.029) Å.[30]

2.2. Photoluminescence of Gd^{3+} in $LaBO_3$ and $Y_2[B_2(SO_4)_6]$

Figure 1a shows the relevant energy level scheme of Gd^{3+} used as a model system to probe various impacts on a nonradiative thermalization rate. The photoluminescence excitation and emission spectra of $LaBO_3$:Gd^{3+} (2 mol%) and $Y_2[B_2(SO_4)_6]$:Gd^{3+} (2 mol%) at 83 K are depicted in Figure 1b,c. The emission spectra are dominated by a sharp zero-phonon line (ZPL) at λ_{em} = 310.0 nm ($LaBO_3$:Gd^{3+}) and λ_{em} = 310.2 nm ($Y_2[B_2(SO_4)_6]$:Gd^{3+}), respectively, which is assigned to the radiative $^6P_{7/2} \rightarrow {}^8S_{7/2}$ transition of Gd^{3+}. The excitation spectra recorded upon monitoring the $^6P_{7/2} \rightarrow {}^8S_{7/2}$ transition of Gd^{3+} at around 310 nm reveal excitation transitions into the $^6I_{J'}$ (J' = 7/2–17/2) levels and the $^6D_{9/2}$ level of Gd^{3+}.

In both emission spectra, also vibronic fine structure is detectable despite the particularly weak vibronic coupling of Gd^{3+} with its $4f^7$ configuration among the trivalent lanthanoid ions.[38–40] The energies of the vibronic bands with respect to the zero-phonon line (see Figure 1c,d) are in excellent agreement with the reported infrared absorption bands of $LaBO_3$ and $Y_2[B_2(SO_4)_6]$.[30,41] The vibronic bands with maximum separation of 1275 cm^{-1} ($LaBO_3$:Gd^{3+}) and 1215 cm^{-1} ($Y_2[B_2(SO_4)_6]$:Gd^{3+}), respectively, are assigned to coupling to the asymmetric B—O stretching vibration.[30,41] The lower value in the borosulfate compared to the borate indicates a slightly weaker B—O bond, in agreement with the expected more ionic nature of the respective bond and the weaker σ-donating nature of the oxygen atoms in the borosulfate compared to the orthoborate.

Figure 2 shows the photoluminescence decay traces of the $^6P_{7/2}$ level of Gd^{3+} in $LaBO_3$:Gd^{3+} (2 mol%) and $Y_2[B_2(SO_4)_6]$:Gd^{3+} (2 mol%), respectively, recorded upon pulsed excitation into the $^6P_{5/2}$ level of Gd^{3+} at 8 K. Both decay curves show purely single-exponential behavior as also the residual plots of the fitting functions clearly indicate. The decay rates of the $^6P_{7/2}$ level can be identified as purely radiative because the large energy gap between $^6P_{7/2}$ and the next lower-lying level (the $^8S_{7/2}$ ground level) prevents nonradiative

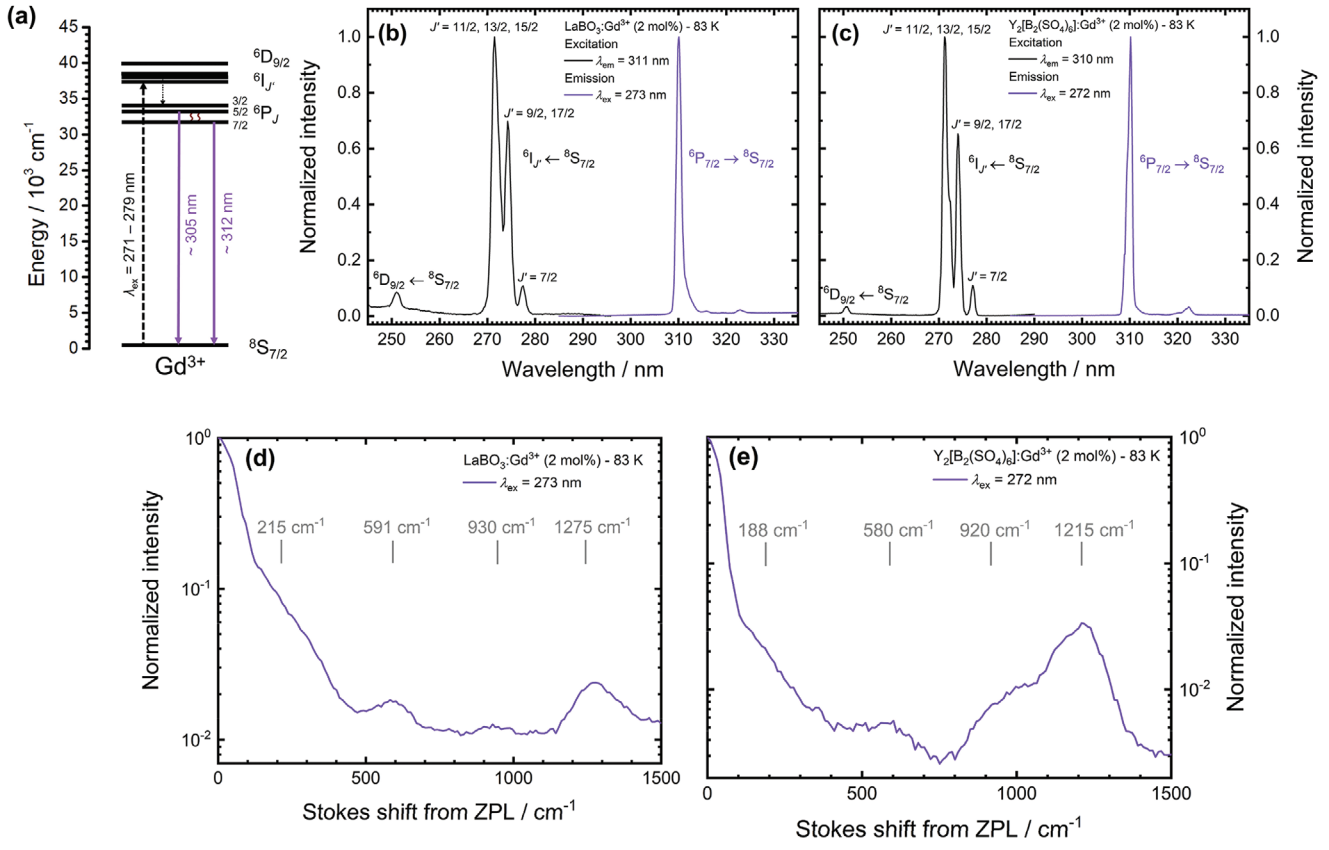

Figure 1. a) Relevant part of the energy level scheme of Gd^{3+} ($4f^7$). Curly arrows indicate the nonradiative transitions between the $^6P_{7/2}$ and $^6P_{5/2}$ levels. Photoluminescence excitation and emission spectra of b) $LaBO_3$:Gd^{3+} (2 mol%) and c) $Y_2[B_2(SO_4)_6]$:Gd^{3+} (2 mol%) at 83 K. Set emission and excitation wavelengths for recording of the spectra are indicated. The observed vibronic fine structure in the emission spectra is plotted in an energy scale with respect to the zero-phonon line (ZPL) for d) $LaBO_3$:Gd^{3+} and e) $Y_2[B_2(SO_4)_6]$:Gd^{3+}. Spectrally resolved vibronic lines are indicated.

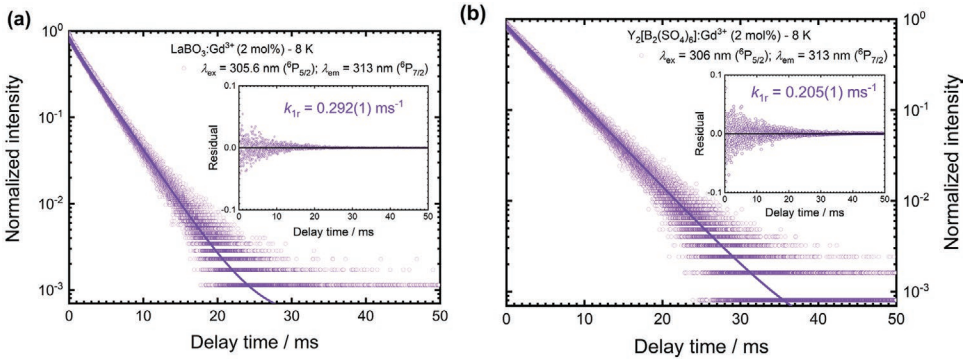

Figure 2. Photoluminescence decay curves of Gd^{3+} recorded upon excitation into the $^6P_{5/2}$ level and monitoring the emission of the $^6P_{7/2}$ level at 8 K of a) $LaBO_3$:Gd^{3+} (2 mol%) and b) $Y_2[B_2(SO_4)_6]$:Gd^{3+} (2 mol%). The solid lines represent fits to single-exponential decay functions, while the insets depict the corresponding residual plots.

processes. The radiative rates are rather small ($LaBO_3$:Gd^{3+}: $k_r(^6P_{7/2}) = (0.292 \pm 0.001)$ ms^{-1} and $Y_2[B_2(SO_4)_6]$:Gd^{3+}: $k_r(^6P_{7/2}) = (0.205 \pm 0.001)$ ms^{-1}) as is often observed for Gd^{3+}.[42] This reveals the strong magnetic dipolar nature of the $^6P_{7/2} \rightarrow {}^8S_{7/2}$ transition, as also implied by the high reduced $\|\langle \mathbf{L} + g\mathbf{S}\rangle\|^2$ matrix element ($\|\langle \mathbf{L} + g\mathbf{S}\rangle\|^2 = 0.2704$) for the magnetic dipole transition compared to the small values for the higher-rank unit tensor matrix elements ($\|\langle U^{(2)}\rangle\|^2 = 0.0012$; $\|\langle U^{(4)}\rangle\|^2 < 0.0001$; and $\|\langle U^{(6)}\rangle\|^2 < 0.0001$),[43] which govern the probability of the induced $4f^n$–$4f^n$ electric dipole transitions in Judd–Ofelt theory.[44] The strong magnetic dipolar nature of the $^6P_{7/2} \rightarrow {}^8S_{7/2}$ transition of Gd^{3+} has also been recently experimentally demonstrated by systematically varying the refractive index of the solvent surrounding Gd^{3+} in shelled β-$NaYF_4$ nanocrystals to tune the radiative decay rate.[45] The higher radiative emission rate of the $^6P_{7/2}$ level of Gd^{3+} in $LaBO_3$ compared to $Y_2[B_2(SO_4)_6]$ is also a reflection of the slightly more covalent nature of the Gd—O bond in the orthoborate, which mostly affects the Ω_2 Judd–Ofelt parameter connected to the $\|\langle U^{(2)}\rangle\|^2$ reduced matrix element.

2.3. Temperature-Dependent Nonradiative Coupling of the ^6P_J (J = 5/2, 7/2) Levels of Gd^{3+}

To investigate thermal coupling between the ^6P_J levels, temperature-dependent emission spectra of $LaBO_3$:Gd^{3+} and $Y_2[B_2(SO_4)_6]$:Gd^{3+} were recorded upon excitation into the $^6I_{J'}$ (J' = 11/2–15/2) level at 272 nm (see **Figure 3**a,b). With increasing temperature, a second emission peak at around 304 nm emerges in the spectra of both compounds, which stems from the thermal population of the higher excited $^6P_{5/2}$ level of Gd^{3+}. The LIRs between these levels reveal a deviation from Boltzmann behavior and emergence of a temperature-independent plateau below 150 K (see Figure 3c,d). The constant LIRs imply a decoupling of the two excited ^6P_J (J = 5/2, 7/2) levels of Gd^{3+}, which is a consequence of competition between radiative decay from the $^6P_{5/2}$ level to the $^8S_{7/2}$ ground level and nonradiative $^6P_{5/2}$–$^6P_{7/2}$ relaxation giving rise to a relative intensity of the $^6P_{5/2}$ emission that is higher than expected based on Boltzmann equilibrium. At the same time, faster radiative decay from the lower energetic $^6P_{7/2}$ level compared to the nonradiative (multiphonon) absorption rate into the higher excited $^6P_{5/2}$ level is slowed down at these low temperatures. This becomes evident from the theoretical temperature dependence of multiphonon relaxation[21,22]

$$k_{nr}^{abs}(T) = g_2 k_{nr}(0)\langle n\rangle^p \tag{1}$$

with $g_2 = 6$ as the J degeneracy of the $^6P_{5/2}$ level, $k_{nr}(0)$ as an intrinsic nonradiative rate governed by the properties of the electronic transition as well as coupling with resonant vibrations, and

$$\langle n\rangle = \frac{1}{\exp\left(\frac{\hbar\omega_{ph}}{k_B T}\right) - 1} \tag{2}$$

as the average thermal occupation number of phonons of energy $\hbar\omega_{ph}$ at the temperature T, and k_B as the Boltzmann constant. The exponent p denotes the expected number of effective phonon modes of this energy to bridge the energy gap between the two excited levels, i.e., $\Delta E_{21} = p\hbar\omega_{ph}$.

In the case of Gd^{3+}, the interlevel energy gap derived from the luminescence spectra (see Figure 3a,b) is in the order of 600–630 cm^{-1}, which can be resonantly bridged by a single phonon mode of both $LaBO_3$ and $Y_2[B_2(SO_4)_6]$. This allows a p = 1 (one-phonon) thermalization for Gd^{3+} doped into these host compounds. The kinetics of the two thermally coupled excited levels in the steady-state regime gives the generalized temperature dependence of the LIR, $R_{21}(T)$[14,16]

$$R_{21}(T) = C\frac{\alpha_{a2}k_{1r} + g_2 k_{nr}(0)\langle n\rangle^p}{(1-\alpha_{a2})k_{2r} + g_1 k_{nr}(0)\left(1+\langle n\rangle\right)^p} \tag{3}$$

with $C = k_{2r}/k_{1r}$ in the specific case of Gd^{3+}, k_{1r} and k_{2r} as the radiative rates of the $^6P_{7/2}$ ($|1\rangle$) and $^6P_{5/2}$ ($|2\rangle$) level, respectively, and α_{a2} as the so-called feeding ratio from the auxiliary level $^6I_{17/2}$ ($|a\rangle$) initially populated during lamp excitation. This formula evolves into the conventional Boltzmann law if the nonradiative rates dominate over the radiative rates,[14] which is the case at higher temperatures (see also Figure 3c,d). Under the assumption of

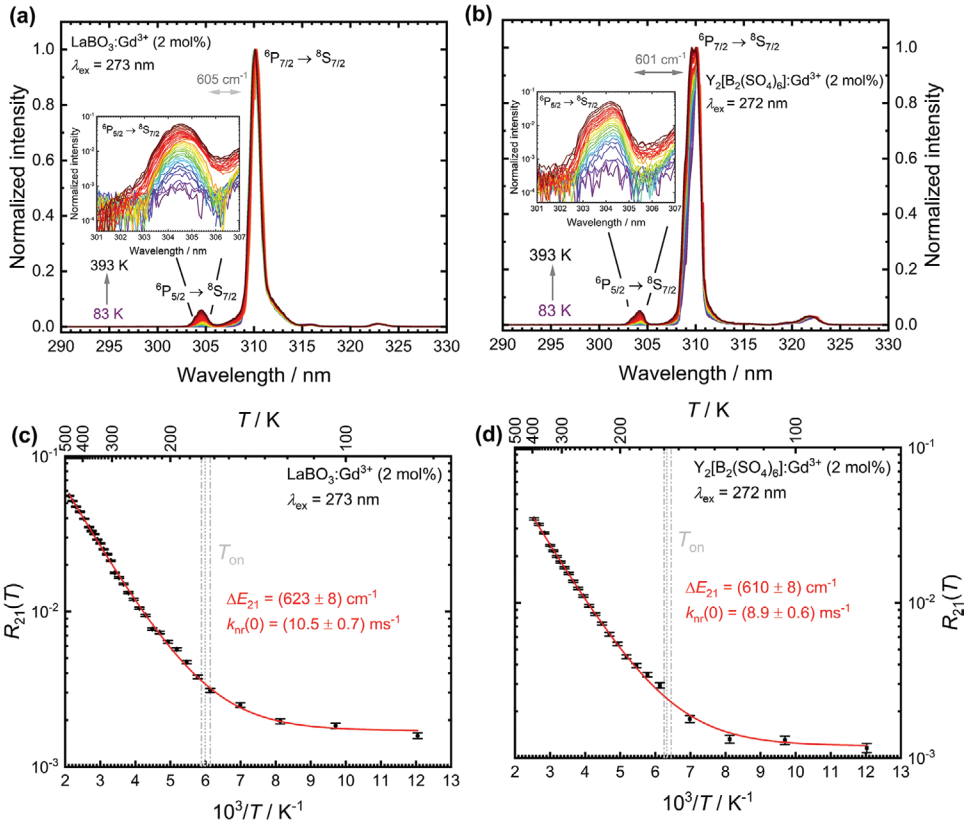

Figure 3. Temperature-dependent photoluminescence spectra of a) $LaBO_3:Gd^{3+}$ (2 mol%) and b) $Y_2[B_2(SO_4)_6]:Gd^{3+}$ (2 mol%) upon excitation into the $^6I_{J'}$ levels (J' = 11/2–15/2; λ_{ex} = 272–273 nm) of Gd^{3+}. The insets depict the evolution of the higher energetic $^6P_{5/2}$ ($|2\rangle$) → $^8S_{7/2}$ ($|0\rangle$) emission in the regarded temperature range. The temperature-dependent luminescence intensity ratios (LIRs) $R_{21}(T)$ between the intensities of the $^6P_{5/2}$ ($|2\rangle$) → $^8S_{7/2}$ ($|0\rangle$) and $^6P_{7/2}$ ($|1\rangle$) → $^8S_{7/2}$ ($|0\rangle$) radiative transitions are depicted below for c) $LaBO_3:Gd^{3+}$ (2 mol%) and d) $Y_2[B_2(SO_4)_6]:Gd^{3+}$ (2 mol%). Note the logarithmic scale on the y axis. The red lines represent least-squares fits to Equation (4). Onset temperatures for the Boltzmann behavior (see Equation (6)) with propagated uncertainties are also depicted.

dominant feeding of the higher excited level $|2\rangle$, i.e., $\alpha_{a2} \to 1$ and with $p = 1$, it is possible to simplify Equation (3) to

$$R_{21}(T) = \frac{k_{2r}}{g_1 k_{nr}(0)} + \left(\frac{g_2 k_{2r}}{g_1 k_{1r}} - \frac{k_{2r}}{g_1 k_{nr}(0)}\right)\exp\left(-\frac{\Delta E_{21}}{k_B T}\right) \equiv B + (A - B)\exp\left(-\frac{\Delta E_{21}}{k_B T}\right) \quad (4)$$

which is just a modified Boltzmann law with constant low-temperature offset. As becomes evident from Figure 3c, Equation (4) fits the measured data very well and indicates the validity of the approximations. This is additionally confirmed by the close agreement between the energy gaps from the fits and the values extracted from the luminescence spectra. From the fitting parameters A and B, it is possible to extract the intrinsic nonradiative rate and thus, gain information about the electronic influence of the local ligand coordination on the nonradiative coupling between the two excited ^6P_J levels of Gd^{3+} in the host compounds $LaBO_3$ and $Y_2[B_2(SO_4)_6]$

$$k_{nr}(0) = \frac{A}{B}\frac{k_{1r}}{g_2} \quad (5)$$

With the radiative decay rates of the lower excited $^6P_{7/2}$ level of Gd^{3+} (see Figure 2a,b) and the A and B values from the fitting procedure, we derive an intrinsic nonradiative coupling rate of k_{nr} (0) = (10.5 ± 0.7) ms^{-1} for $LaBO_3:Gd^{3+}$ and k_{nr} (0) = (8.9 ± 0.6) ms^{-1} for $Y_2[B_2(SO_4)_6]:Gd^{3+}$ (see Figure 3c,d). Both the covalence of the lanthanoid–ligand bond and the average Gd—O bond lengths have an impact on nonradiative rates. The slightly higher value in the orthoborate implies that the longer average Gd—O distances in the orthoborate do not have the major influence on the intrinsic nonradiative rate as this would give rise to a lower intrinsic nonradiative rate in the orthoborate. The observed trend in the intrinsic nonradiative rates must therefore originate from a lower degree of covalence of the Gd—O bond and the weaker σ-donating character of the borosulfate anions, which results in a lower nonradiative transition rate in that compound. A similar explanation was given for the difference in the radiative decay rates above (see Figure 2). However, the similarity of the two nonradiative transition rates also shows that this effect is rather subtle. Future extensive structure–property studies are required to establish general influences of the chemical composition and structurally imposed lanthanoid–ligand distances on nonradiative rates.

2.4. Nature of the Nonradiative Thermalization and Implications for Gd^{3+} as a Luminescent Thermometer

The derived intrinsic nonradiative coupling rates of the ^6P_J levels of Gd^{3+} are very small, especially since resonant bridging via a single phonon mode is possible in these two host compounds. It is insightful to compare these results to other lanthanide ions. For example, the intrinsic nonradiative rate for the coupling of the green-emitting $^2H_{11/2}$ and $^4S_{3/2}$ levels in YVO_4:Er^{3+} ($k_{nr}(0) = 3 \times 10^4$ ms^{-1}) is over three orders of magnitude higher than for Gd^{3+}, while both the energy gap and the number of phonons needed to bridge the gap are very similar.[46] This implies that the nonradiative rate for coupling between the ^6P_J levels of Gd^{3+} is fundamentally small, and hints to the relevance of selection rules, as was originally also proposed by Weber.[47] Given the high reduced $\|\langle \mathbf{L} + g\mathbf{S}\rangle\|^2$ matrix element for the nonradiative $^6P_{5/2} \leftrightarrow {}^6P_{7/2}$ transition of Gd^{3+} ($\|\langle \mathbf{L} + g\mathbf{S}\rangle\|^2 = 5.7412$) compared to the higher-rank unit tensor matrix elements ($\|\langle U^{(2)}\rangle\|^2 = 0.0180$; $\|\langle U^{(4)}\rangle\|^2 < 0.0001$; and $\|\langle U^{(6)}\rangle\|^2 < 0.0001$),[48,49] an intrinsically dominant magnetic dipolar contribution is expected. According to theory, the nonradiative rate of Gd^{3+} is a factor of 10^{-4}–10^{-5} lower than the rate of an induced electric-dipole-type nonradiative transition.[14a,24,25] This is in very good agreement with the previously mentioned experimentally measured nonradiative thermalization rate of the green-emitting levels of Er^{3+} in YVO_4 that has a dominant electric dipolar character as also implied by the respective reduced matrix elements ($\|\langle U^{(2)}\rangle\|^2 < 0.0001$; $\|\langle U^{(4)}\rangle\|^2 = 0.2002$; and $\|\langle U^{(6)}\rangle\|^2 = 0.0097$).[48,49] Another instructive example is the gap between the NIR-emitting $^4F_{5/2}$ and $^4F_{3/2}$ levels of Nd^{3+} ($\Delta E \approx 1000$ cm^{-1}) in $LaPO_4$, which can also be resonantly bridged by a single phonon mode in that host compound. The corresponding intrinsic nonradiative transition rate was reported as $k_{nr}(0) \approx 60$ ms^{-1}, which appears small for a resonant one-phonon transition compared to the previously discussed example of YVO_4:Er^{3+} and is rather similar to the found nonradiative rates of Gd^{3+} within this work.[17,46] Again, this is understandable given the substantial magnetic dipolar nature of the respective nonradiative transition ($\|\langle \mathbf{L} + g\mathbf{S}\rangle\|^2 = 9.6446$) compared to the respective reduced unit tensor matrix elements ($\|\langle U^{(2)}\rangle\|^2 = 0.0795$; $\|\langle U^{(4)}\rangle\|^2 = 0.0523$; and $\|\langle U^{(6)}\rangle\|^2 < 0.0001$).[48–50] This also indicates a strong magnetic dipolar character of the nonradiative transition.

A quantitative correlation between the intrinsic nonradiative transition rates and the average bond length between the lanthanoid atoms and oxygen ligands is to be taken with caution as the bond lengths are also temperature dependent and would formally require the structural data at low temperatures ($T < 10$ K) to make such a comparison reliable. Moreover, the expected power dependences of the intrinsic nonradiative transition rates on the lanthanoid-to-ligand distance ($k_{nr}(0) \sim d^{-6}$ for an electric dipolar and $k_{nr}(0) \sim d^{-4}$ for a magnetic dipolar transition) only strictly apply to the case of a point dipole, which is a good approximation for the electronic $4f^n$–$4f^n$ transitions given the shielded nature of the 4f orbitals from their chemical environment but not for the phonon modes, which involve displacement of nuclei relative to the valence electron density of cations and anions surrounding and including the lanthanoid ion in the host lattice.[14,24,25]

From the intrinsic nonradiative transition rates $k_{nr}(0)$, it is also possible to estimate the onset temperature for kinetic sustainment of Boltzmann equilibrium and, thus, the dynamic working range as a luminescent thermometer. It is defined by the condition $k_{nr}^{abs}(T = T_{on}) = k_{1r}$, i.e., it is the threshold at which the nonradiative absorption rate from the lower excited level $|1\rangle$ to the higher excited level $|2\rangle$ becomes similar to the radiative depopulation rate of level $|1\rangle$. Usage of Equations (1) and (2) leads to

$$T_{on} = \frac{\Delta E_{21}}{k_B \ln\left(1 + \frac{g_2 k_{nr}(0)}{k_{1r}}\right)} = \frac{\Delta E_{21}}{k_B \ln\left(1 + \frac{A}{B}\right)} \quad (6)$$

With the data from the time-resolved measurements (see Figure 2) and the temperature-dependent LIR, it follows T_{on} = 162 K for $LaBO_3$:Gd^{3+} and T_{on} = 156 K for $Y_2[B_2(SO_4)_6]$:Gd^{3+}. Although they should be regarded as estimate values, the onset temperatures are in line with the observed trend of the evolution of the LIR with temperature (see Figure 3c,d). Despite the slightly higher intrinsic nonradiative transition rate between the ^6P_J (J = 7/2, 5/2) levels of Gd^{3+} in $LaBO_3$ based on the more covalent Gd—O bond, the onset temperature for Boltzmann behavior of the measured LIR is still higher than that of $Y_2[B_2(SO_4)_6]$:Gd^{3+}. This is related to the compensating effect of a higher radiative depopulation rate of the $^6P_{7/2}$ level (see Figure 2a) and the consequent lower ratio. In general, careful selection of the host compound and tuning of the covalence of the lanthanoid–ligand bond thus offer the possibility of extending the dynamic range of a luminescent Boltzmann thermometer.

It is again instructive to compare to the example of Er^{3+} in YVO_4 and thermal coupling between the green-emitting $^2H_{11/2}$ and $^4S_{3/2}$ levels. Following Equation (6), the onset temperature of Boltzmann equilibrium in YVO_4:Er^{3+} is 113 K, which is in excellent agreement to the observed onset at around 100 K.[46] Thus, an electric dipolar nonradiative transition kinetically extends the temperature range of a luminescent Boltzmann thermometer enormously because of the over three orders of magnitude higher nonradiative transition rates. In turn, this means that, although the energy gap of around 630 cm^{-1} is thermodynamically suited for the measurement of temperatures in the range of room temperature,[14] the dominant magnetic dipolar nature of the nonradiative coupling between the ^6P_J (J = 7/2, 5/2) levels of Gd^{3+} can yet pose fundamental kinetic limitations to the application of this ion over a wide temperature range for remote temperature sensing.

3. Conclusion

We investigated the impact of the ligand field on the nonradiative coupling of the excited ^6P_J (J = 5/2, 7/2) levels of Gd^{3+}. For that purpose, we doped Gd^{3+} into $LaBO_3$ and $Y_2[B_2(SO_4)_6]$. Both host compounds offer low symmetric coordination spheres for lanthanoid dopants, which differ in the average lanthanoid-to-oxygen distance. The low-temperature luminescence spectra (T = 83 K) in the UV range reveal the presence of weak vibronic fine structure next to the most intense zero-phonon

line of the $^6P_{7/2} \rightarrow {}^8S_{7/2}$ transition of Gd^{3+}. The lower value of the highest-energetic vibrational mode (1215 cm^{-1}) in the case of the borosulfate confirms the weaker and less covalent chemical bond between Gd^{3+} and the surrounding O^{2-} ions in that compound. Temperature-dependent luminescence spectra and luminescence decay measurements demonstrated that the intrinsic nonradiative rate is slightly higher for $LaBO_3:Gd^{3+}$ due to the higher degree of covalence. This analysis shows that the dynamic working range of a luminescent thermometer can be controlled by careful choice of an appropriate host compound and tailoring of the nature of the surrounding ligand field of a lanthanoid ion. These fundamental aspects are highly relevant for the kinetically controlled design and optimization of luminescent thermometers in general.

Compared to the well-established thermally coupled $^4S_{3/2}$ and $^2H_{11/2}$ levels in Er^{3+}, the nonradiative transition between the $^6P_{7/2}$ and $^6P_{5/2}$ levels in Gd^{3+} is over three orders of magnitude slower. This is caused by the strong magnetic dipole character of coupling in Gd^{3+}, while coupling in Er^{3+} has a dominant electric dipole character. As a result, Boltzmann thermometry in $LaBO_3:Gd^{3+}$ and $Y_2[B_2(SO_4)_6]:Gd^{3+}$, respectively, is only possible above at least 160 K compared to a much lower onset value of 100 K for $YVO_4:Er^{3+}$. Similarly, slow nonradiative coupling related to a dominant magnetic dipolar character of the electronic $4f^n$–$4f^n$ transition is known for the $^4F_{5/2}$ and $^4F_{3/2}$ levels in the case of $LaPO_4:Nd^{3+}$. This shows that nonradiative transitions also follow selection rules similar to radiative ones. These insights demonstrate that the choice of the lanthanoid ion, a specific $4f^n$–$4f^n$ transition, and host compound are clearly relevant for the targeted control of the dynamic working range of a luminescent Boltzmann thermometer.

4. Experimental Section

Synthesis of $La_{0.98}Gd_{0.02}BO_3$: Microcrystalline $La_{0.98}Gd_{0.02}BO_3$ powder was prepared in a conventional solid-state synthesis. La_2O_3 (Merck, 99.9%) was pre-fired at 1000 °C overnight to remove any traces of $La(OH)_3$ or LaOOH and thoroughly mixed in respective amounts with Gd_2O_3 (Highland Chemicals, 99.999%) and H_3BO_3 (Merck, 99.8%) in a mortar for around 10 min. The solid mixture was transferred to an alumina crucible and heated at 300 °C for 3 h. After natural cooling to room temperature, the powder was reground for 10 min, and finally heated at 850 °C for 12 h.

After natural cooling to room temperature, the obtained colorless residue was ground to a fine powder, and its phase purity was verified by X-ray powder diffraction (Philips PW391, Cu Kα1 radiation (λ = 1.54056 Å), U = 40 kV, I = 20 mA, reflection mode). The X-ray diffraction pattern was scanned in a 2θ range between 10° and 80° with a step size of 0.02° (see Figure S1 in the Supporting Information).

Synthesis of $Y_{1.96}Gd_{0.04}[B_2(SO_4)_6]$: $Y_{1.96}Gd_{0.04}[B_2(SO_4)_6]$ was prepared by the synthesis method given in ref. [30]. 0.49 mmol Y_2O_3 (Alfa Aesar, 99.9%) and 0.01 mmol Gd_2O_3 (Applichem, 99.99%)—pre-fired at 1000 °C for 10 h—were added to the superacid $H[B(HSO_4)_4]$ prepared from 1 mmol B_2O_3 (Sigma–Aldrich, 99%), 2.5 mL H_2SO_4 (Merck, 95–97%), and 0.3 mL oleum (VWR, 65% SO_3) prior to the solvothermal synthesis in a sealed silica glass ampoule (length: 15 cm, outer diameter: 1.2 cm, and wall thickness: 0.1 cm) in a muffle furnace at 300 °C for 80 h with ramps of 100 °C h^{-1}. The ampoule was opened after cooling with liquid nitrogen (Caution! During and even after the reaction the ampoules are under remarkable pressure and must therefore be handled with great care!). After decantation of the excess sulfuric acid, it was heated at 300 °C for 14 h inside a muffle furnace. The dry and hygroscopic product was taken out of the furnace at 150 °C and immediately transferred into an argon-filled glovebox. For further investigations, it was stored under inert conditions.

Phase purity was verified by X-ray powder diffraction (see Figure S1 in the Supporting Information). The sample was ground and filled into a Hilgenberg glass capillary (outer diameter: 0.3 mm and wall thickness: 0.01 mm) inside the argon-filled glovebox. The data were collected with a Bruker D8 Advance diffractometer with Cu Kα radiation (λ = 1.54184 Å) with a 1D LynxEye detector, steps of 0.02°, and transmission geometry. The generator was driven at 40 kV and 40 mA. The background at lower diffraction angles was due to the absorption of the glass capillary.

Optical Spectroscopy and Temperature-Dependent Measurements: Emission and excitation spectra were acquired on an Edinburgh FLS920 spectrofluorometer equipped with a 450 W continuous Xe lamp, a 0.25 m double Littrow-configuration grating monochromator blazed at 300 nm, and a Hamamatsu R928 photomultiplier tube (PMT) for photon detection. All emission spectra were corrected for grating efficiency and detector sensitivity, while the excitation spectra were additionally corrected with respect to the lamp intensity. Temperature-dependent measurements between 77 and 473 K were performed by placing the sample into a Linkam THMS600 microscope stage (±0.1 °C temperature stability). The temperature was externally controlled by a thermocouple in immediate contact with the sample holder. Photoluminescence decay curves at 8 K were measured with an Ekspla NT342B optical parametric oscillator (OPO) laser with a repetition rate of 10 Hz, a Triax 550 monochromator, and a Hamamatsu R928 PMT. The laser synchronization and detection signals were recorded with a PicoQuant Timeharp 260 time-correlated single-photon counting module. For those measurements, the sample was placed into a cold finger He liquid flow cryostat (Oxford Instruments) with an external temperature control unit.

Supporting Information

Supporting Information is available from the Wiley Online Library or from the author.

Acknowledgements

P.N. and M.H. contributed equally to this work. H.A.H., P.N., M.H., and E.T. thank the Deutsche Forschungsgemeinschaft (DFG) for generous support (Project HO 4503/5-1).

Open access funding enabled and organized by Projekt DEAL.

Conflict of Interest

The authors declare no conflict of interest.

Data Availability Statement

The data that support the findings of this study are available from the corresponding author upon reasonable request.

Keywords

borates, borosulfates, Gd^{3+}, luminescence thermometry, nonradiative transitions, structure–property relationship

Received: January 10, 2022
Revised: March 8, 2022
Published online: April 7, 2022

[1] a) D. Jaque, F. Vetrone, *Nanoscale* **2012**, *4*, 4301; b) C. D. S. Brites, P. P. Lima, N. J. O. Silva, A. Millán, V. S. Amaral, F. Palacio, L. D. Carlos, *Nanoscale* **2012**, *4*, 4799; c) X. Wang, O. S. Wolfbeis, R. J. Meier, *Chem. Soc. Rev.* **2013**, *42*, 7834.

[2] a) C. D. S. Brites, S. Balabhadra, L. D. Carlos, *Adv. Opt. Mater.* **2019**, *7*, 1801239; b) M. Dramićanin, *Luminescence Thermometry—Methods, Materials, and Applications*, Woodhead Publishing (Elsevier), Duxford **2018**; c) M. D. Dramićanin, *J. Appl. Phys.* **2020**, *128*, 040902.

[3] a) S. Yakunin, B. M. Benin, Y. Shynkarenko, O. Nazarenko, M. I. Bodnarchuk, D. N. Dirin, C. Hofer, S. Cattaneo, M. V. Kovalenko, *Nat. Mater.* **2019**, *18*, 846; b) V. Morad, S. Yakunin, B. M. Benin, Y. Shynkarenko, M. J. Grotevent, I. Shorubalko, S. C. Boehme, M. V. Kovalenko, *Adv. Mater.* **2021**, *33*, 2007355.

[4] Y. Xiao, C. Wan, A. Shahsafi, J. Salman, Z. Yu, R. Wambold, H. Mei, B. E. R. Perez, W. Derdeyn, C. Yao, M. A. Kats, *Laser Photonics Rev.* **2020**, *14*, 1900443.

[5] a) H. D. A. Santos, I. Zabala Gutiérrez, Y. Shen, J. Lifante, E. Ximendes, M. Laurenti, D. Méndez-González, S. Melle, O. G. Calderón, E. López Cabarcos, N. Fernández, I. Chaves-Coira, D. Lucena-Agell, L. Monge, M. D. Mackenzie, J. Marqués-Hueso, C. M. S. Jones, C. Jacinto, B. del Rosal, A. K. Kar, J. Rubio-Retama, D. Jaque, *Nat. Commun.* **2020**, *11*, 2933; b) C. Gota, K. Okabe, T. Funatsu, Y. Harada, S. Uchiyama, *J. Am. Chem. Soc.* **2009**, *131*, 2766; c) K. Okabe, N. Inada, C. Gota, Y. Harada, T. Funatsu, S. Uchiyama, *Nat. Commun.* **2012**, *3*, 705; d) T. Hayashi, N. Fukuda, S. Uchiyama, N. Inada, *PLoS One* **2015**, *10*, e0117677.

[6] a) E. Ximendes, A. Benayas, D. Jaque, R. Marin, *ACS Nano* **2021**, *15*, 1917; b) A. Bednarkiewicz, L. Marciniak, L. D. Carlos, D. Jaque, *Nanoscale* **2020**, *12*, 14405; c) A. Bednarkiewicz, J. Drabik, K. Trejgis, D. Jaque, E. Ximendes, L. Marciniak, *Appl. Phys. Rev.* **2021**, *8*, 011317.

[7] a) R. G. Geitenbeek, P. T. Prins, W. Albrecht, A. van Blaaderen, B. M. Weckhuysen, A. Meijerink, *J. Phys. Chem. C* **2017**, *121*, 3503; b) A. Ćirić, J. Aleksić, T. Barudžija, Ž. Antić, V. Đorđević, M. Medić, J. Periša, I. Zeković, M. Mitrić, M. D. Dramićanin, *Nanomaterials* **2020**, *10*, 627.

[8] a) R. G. Geitenbeek, A.-E. Nieuwelink, T. S. Jacobs, B. B. V. Salzmann, J. Goetze, A. Meijerink, B. M. Weckhuysen, *ACS Catal.* **2018**, *8*, 2397; b) I. K. Ravenhorst, R. G. Geitenbeek, M. J. Eerden, J. van Tijn Omme, H. H. Peréz Garza, F. Meirer, A. Meijerink, B. M. Weckhuysen, *ChemCatChem* **2019**, *11*, 5505; c) T. Hartman, R. G. Geitenbeek, G. T. Whiting, B. M. Weckhuysen, *Nat. Catal.* **2019**, *2*, 986; d) T. Hartman, R. G. Geitenbeek, C. S. Wondergem, W. van der Stam, B. M. Weckhuysen, *ACS Nano* **2020**, *14*, 3725.

[9] a) A. M. Kaczmarek, H. S. Jena, C. Krishnaraj, H. Rijckaert, S. K. P. Veerapandian, A. Meijerink, P. van der Voort, *Angew. Chem.* **2021**, *60*, 3727; b) A. M. Kaczmarek, H. S. Jena, C. Krishnaraj, H. Rijckaert, S. K. P. Veerapandian, A. Meijerink, P. van der Voort, *Angew. Chem., Int. Ed.* **2021**, *133*, 3771.

[10] M. Back, J. Ueda, H. Nambu, M. Fujita, A. Yamamoto, H. Yoshida, H. Tanaka, M. G. Brik, S. Tanabe, *Adv. Opt. Mater.* **2021**, *9*, 2100033.

[11] T. P. van Swieten, T. van Omme, D. J. van den Heuvel, S. J. W. Vonk, R. G. Spruit, F. Meirer, H. H. P. Garza, B. M. Weckhuysen, A. Meijerink, F. T. Rabouw, R. G. Geitenbeek, *ACS Appl. Nano Mater.* **2021**, *4*, 4208.

[12] M. A. Hernández-Rodríguez, C. D. S. Brites, G. Antorrena, R. Piñol, R. Cases, L. Pérez-García, M. Rodrigues, J. A. Plaza, N. Torras, I. Díez, A. Millán, L. D. Carlos, *Adv. Opt. Mater.* **2020**, *8*, 2000312.

[13] a) C. D. S. Brites, X. Xie, M. L. Debasu, X. Qin, R. Chen, W. Huang, J. Rocha, X. Liu, L. D. Carlos, *Nat. Nanotechnol.* **2016**, *11*, 851; b) C. D. S. Brites, M. C. Fuertes, P. C. Angelomé, E. D. Martínez, P. P. Lima, G. J. A. A. Soler-Illia, L. D. Carlos, *Nano Lett.* **2017**, *17*, 4746; c) A. R. N. Bastos, C. D. S. Brites, P. A. Rojas-Gutierrez, C. DeWolf, R. A. S. Ferreira, J. A. Capobianco, L. D. Carlos, *Adv. Funct. Mater.* **2019**, *29*, 1905474; d) A. R. N. Bastos, C. D. S. Brites, P. A. Rojas-Gutierrez, R. A. S. Ferreira, R. L. Longo, C. DeWolf, J. A. Capobianco, L. D. Carlos, *Nanoscale* **2020**, *12*, 24169.

[14] a) M. Suta, A. Meijerink, *Adv. Theory Simul.* **2020**, *3*, 2000176; b) D. Yu, H. Li, D. Zhang, Q. Zhang, A. Meijerink, M. Suta, *Light: Sci. Appl.* **2021**, *10*, 236.

[15] a) F. Vetrone, R. Naccache, A. Zamarrón, A. La Juarranz de Fuente, F. Sanz-Rodríguez, L. Martinez Maestro, E. Martín Rodriguez, D. Jaque, J. García Solé, J. A. Capobianco, *ACS Nano* **2010**, *4*, 3254; b) S. Balabhadra, M. L. Debasu, C. D. S. Brites, R. A. S. Ferreira, L. D. Carlos, *J. Phys. Chem. C* **2017**, *121*, 13962; c) A. Ćirić, T. Gavrilović, M. D. Dramićanin, *Crystals* **2021**, *11*, 189; d) A. Skripka, D. Méndez González, R. Marin, E. Ximendes, B. del Rosal, D. Jaque, P. Rodriguez Sevilla, *Nanoscale Adv.* **2021**, *3*, 6310.

[16] R. G. Geitenbeek, H. W. de Wijn, A. Meijerink, *Phys. Rev. Appl.* **2018**, *10*, 64006.

[17] M. Suta, Ž. Antić, V. Đorđević, S. Kuzman, M. D. Dramićanin, A. Meijerink, *Nanomaterials* **2020**, *10*, 543.

[18] A. Skripka, A. Benayas, C. D. S. Brites, I. R. Martín, L. D. Carlos, F. Vetrone, *Nano Lett.* **2020**, *20*, 7648.

[19] a) R. S. Meltzer, S. P. Feofilov, B. Tissue, H. B. Yuan, *Phys. Rev. B* **1999**, *60*, R14012; b) D. Toptygin, *J. Fluoresc.* **2003**, *13*, 201; c) T. Senden, F. T. Rabouw, A. Meijerink, *ACS Nano* **2015**, *9*, 1801.

[20] a) E. M. Purcell, *Phys. Rev.* **1946**, *69*, 37; b) D. Kleppner, *Phys. Rev. Lett.* **1981**, *47*, 233.

[21] L. A. Riseberg, H. W. Moos, *Phys. Rev. Lett.* **1967**, *19*, 1423.

[22] L. A. Riseberg, H. W. Moos, *Phys. Rev.* **1968**, *174*, 429.

[23] R. Englman, J. Jortner, *Mol. Phys.* **1970**, *18*, 145.

[24] V. L. Ermolaev, E. B. Sveshnikova, *J. Lumin.* **1979**, *20*, 387.

[25] E. B. Sveshnikova, V. L. Ermolaev, *Opt. Spectrosc.* **2011**, *111*, 34.

[26] J. M. F. van Dijk, M. F. H. Schuurmans, *J. Chem. Phys.* **1983**, *78*, 5317.

[27] F. T. Rabouw, P. T. Prins, P. Villanueva-Delgado, M. Castelijns, R. G. Geitenbeek, A. Meijerink, *ACS Nano* **2018**, *12*, 4812.

[28] M. A. El-Sayed, *J. Chem. Phys.* **1963**, *38*, 2834.

[29] M. Kraft, C. Würth, V. Muhr, T. Hirsch, U. Resch-Genger, *Nano Res.* **2018**, *11*, 6360.

[30] P. Netzsch, M. Hämmer, P. Gross, H. Bariss, T. Block, L. Heletta, R. Pöttgen, J. Bruns, H. Huppertz, H. A. Höppe, *Dalton Trans.* **2019**, *48*, 4387.

[31] a) P. Netzsch, P. Gross, H. Takahashi, H. A. Höppe, *Inorg. Chem.* **2018**, *57*, 8530; b) J. Bruns, H. A. Höppe, M. Daub, H. Hillebrecht, H. Huppertz, *Chem. - Eur. J.* **2020**, *26*, 7966; c) P. Netzsch, R. Stroh, F. Pielnhofer, I. Krossing, H. A. Höppe, *Angew. Chem.* **2021**, *133*, 10738; d) P. Netzsch, R. Stroh, F. Pielnhofer, I. Krossing, H. A. Höppe, *Angew. Chem., Int. Ed.* **2021**, *60*, 10643; e) P. Netzsch, F. Pielnhofer, R. Glaum, H. A. Höppe, *Chem. - Eur. J.* **2020**, *26*, 14745.

[32] a) E. M. Levin, R. S. Roth, J. B. Martin, *Am. Mineral.* **1961**, *46*, 1030; b) E. M. Levin, C. R. Robbins, J. L. Waring, *J. Am. Ceram. Soc.* **1961**, *44*, 87.

[33] a) P. Gross, A. Kirchhain, H. A. Höppe, *Angew. Chem.* **2016**, *128*, 4426; b) P. Gross, A. Kirchhain, H. A. Höppe, *Angew. Chem., Int. Ed.* **2016**, *55*, 4353.

[34] J. Weidelt, H. U. Bambauer, *Naturwissenschaften* **1968**, *55*, 342.

[35] F. Goubin, Y. Montardi, P. Deniard, X. Rocquefelte, R. Brec, S. Jobic, *J. Solid State Chem.* **2004**, *177*, 89.

[36] H. Müller-Bunz, T. Nikelski, T. Schleid, *Z. Naturforsch., B: J. Chem. Sci.* **2003**, *58*, 375.

[37] A. Haberer, R. Kaindl, H. Huppertz, *Z. Naturforsch., B: J. Chem. Sci.* **2010**, *65*, 1206.

[38] K.-H. Hellwege, *Ann. Phys.* **1941**, *432*, 529.

[39] a) J. Sytsma, W. van Schaik, G. Blasse, *J. Phys. Chem. Solids* **1991**, *52*, 419; b) J. Sytsma, G. Blasse, *J. Phys. Chem. Solids* **1992**, *53*, 561.

[40] a) A. Ellens, H. Andres, M. L. H. ter Heerdt, R. T. Wegh, A. Meijerink, G. Blasse, *Phys. Rev. B* **1997**, *55*, 180; b) A. Meijerink, *J. Lumin.* **1993**, *55*, 125; c) J. Sytsma, G. Blasse, *J. Lumin.* **1992**, *51*, 283; d) A. Meijerink, C. de Mello Donegá, A. Ellens, J. Sytsma, G. Blasse, *J. Lumin.* **1994**, *58*, 26.
[41] W. C. Steele, J. C. Decius, *J. Chem. Phys.* **1956**, *25*, 1184.
[42] J. Sytsma, G. F. Imbusch, G. Blasse, *J. Chem. Phys.* **1989**, *91*, 1456.
[43] J. A. Detrio, *Phys. Rev. B* **1971**, *4*, 1422.
[44] a) B. R. Judd, *Phys. Rev.* **1962**, *127*, 750; b) G. S. Ofelt, *J. Chem. Phys.* **1962**, *37*, 511.
[45] Z. Wang, T. Senden, A. Meijerink, *J. Phys. Chem. Lett.* **2017**, *8*, 5689.
[46] J. A. Capobianco, P. Kabro, F. S. Ermeneux, R. Moncorgé, M. Bettinelli, E. Cavalli, *Chem. Phys.* **1997**, *214*, 329.
[47] M. J. Weber, *Phys. Rev. B* **1973**, *8*, 54.
[48] W. T. Carnall, G. L. Goodman, K. Rajnak, R. S. Rana, *J. Chem. Phys.* **1989**, *90*, 3443.
[49] M. P. Hehlen, M. G. Brik, K. W. Krämer, *J. Lumin.* **2013**, *136*, 221.
[50] A. A. Kaminskii, G. Boulon, M. Buoncristiani, B. Di Bartolo, A. Kornienko, V. Mironov, *Phys. Status Solidi A* **1994**, *141*, 471.